

8 Week Report

Summer Research Fellowship Program 2024

First Principle Investigation on Fe₂ScZ (Z=Si; Ge; Sn)

July 11, 2025



Report by: Mr. Nimish Sharma
Supervised by: Dr Himanshu Pandey

Contents

1	Introduction	6
1.1	Problem Statement/Motivation	6
2	Theoretical Framework	6
2.1	Density Functional Theory	6
2.1.1	Hohenberg and Kohn Theorem 1	7
2.1.2	Hohenberg and Kohn Theorem 2	7
2.1.3	Kohn-Sham scheme	8
2.1.4	Plane Wave DFT	9
2.2	Heusler Alloys	11
2.2.1	Regular Heusler Alloys	11
2.2.2	Half-Heusler Alloys	11
2.2.3	Inverse Heusler Alloys	11
2.2.4	Properties and Applications	11
2.2.5	Challenges and Innovations	12
3	Softwares	12
3.1	WIEN2k	12
3.1.1	FP-LAPW	12
3.1.2	APW+lo	13
3.2	Quantum Espresso	15
3.2.1	Pseudopotentials	15
3.3	VESTA	15
4	Methodology	16
4.1	Implementation	16
4.1.1	WIEN2k	16
4.1.2	Quantum Espresso	18
4.2	Optimizations	20
4.2.1	WIEN2k	20
4.2.2	Quantum ESPRESSO	21
4.3	Computational Detail	23
4.3.1	WIEN2k	23
4.3.2	Quantum ESPRESSO	23
5	Results	23
5.1	Structure	23
5.2	Magnetic Properties	26
5.3	Mechanical Stability	27
5.3.1	Elastic constants	27
5.3.2	Ductility/Malleability	28
5.3.3	Nature of Bonds	28
5.4	Dynamical Stability	29
5.5	Electronic Properties	31
6	Conclusion	34

List of Figures

1	Jacob's Ladder	8
2	Flow chart for the SCF calculation	9
3	Brillouin Zones for (a) simple cubic (SC), (b) face centered cubic (fcc), (c) body centered cubic (bcc), (d) hexagonal (hex)	10
4	Program flow in WIEN2k	14
5	optimize.job	17
6	Input file for SCF in QE	18
7	Optimization plot for ecut parameter in WIEN2k	20
8	Optimization plot for RKmax parameter in WIEN2k	21
9	Optimization plot for RMT reduction parameter in WIEN2k	21
10	Optimization plot for ecut parameter in QE	22
11	Optimization plot for K points in QE	22
12	(a) Inverse structure of Fe ₂ ScSi (b) Regular structure of Fe ₂ ScSi	23
13	(a) Inverse structure of Fe ₂ ScGe (b) Regular structure of Fe ₂ ScGe	24
14	(a) Inverse structure of Fe ₂ ScSn (b) Regular structure of Fe ₂ ScSn	24
15	Volume optimization plot for Fe ₂ ScSi	25
16	Volume optimization plot for Fe ₂ ScGe	25
17	Volume optimization plot for Fe ₂ ScSn	26
18	Fe ₂ ScSi (regular): (a) Phonon Bandstructure (b) Phonon DOS	29
19	Fe ₂ ScGe (regular): (a) Phonon Bandstructure (b) Phonon DOS	29
20	Fe ₂ ScSn (regular): (a) Phonon Bandstructure (b) Phonon DOS	30
21	Fe ₂ ScSi Bandstructure and DOS: (a) spin up (b) spin down	31
22	Fe ₂ ScGe Bandstructure and DOS: (a) spin up (b) spin down	32
23	Fe ₂ ScSn Bandstructure and DOS: (a) spin up (b) spin down	33

List of Tables

1	Calculated properties for Fe ₂ ScSi, Fe ₂ ScGe, and Fe ₂ ScSn alloys	26
2	Data for Magnetic Moment across PBE, mBJ and HSE potential	27
3	Data for Elastic properties, C_{11} , C_{12} , C_{44} , Bulk Modulus (B_H), Shear Modulus (G_H), Young's Modulus (Y_H), Poisson Ratio (ν_H) and Debye temperature (θ_D)	28
4	Calculated Data for Bandgap in the minority spin	34

Abstract

This project report covers the work done in an in-depth study of Heusler alloys. Softwares like WIEN2k[1] and Quantum Espresso (QE)[2–4] were used to reproduce the findings from a seminal paper on Ti_2VGe [5]. Building upon this progress, further work was carried out on $Fe_2ScSi/Ge/Sn$. The analysis was done on multiple density approximations like Perdew-Burke-Ernzerh Generalized Gradient Approximation (PBE-GGA) for structural optimization, and further modified Becke-Jones (mBJ) and Hybrid functional (HF) exchange-correlation potentials were used to examine properties of the alloy under study. Electronic, magnetic and structural properties were investigated for these heusler alloys. The results revealed interesting electronic properties, contributing to a better understanding of these materials, thereby opening up potential applications of Fe_2Sc -based Heusler alloys in spintronic applications.

1 Introduction

Heusler alloys have been of great scientific interest in modern times due to their outstanding applications in various fields, such as spintronics[6–8], thin-film growth, giant magnetoresistance (GMR), thermoelectric applications and other energy conversion systems, as well as their novel characteristics. Current times have brought the depletion of fossil fuels and various environmental concerns, which pushed scientists to investigate new renewable energy sources.

1.1 Problem Statement/Motivation

Searching for Heusler alloys and stable materials exhibiting half-metallic properties is still daunting for researchers in material sciences. This study aims to overcome the experimental hurdles and narrow the choices among the wide range of material choices, easing the tasks for experimentalists to choose the material. Computational techniques predict half-metallic behaviour for Heusler alloys and a high Curie temperature, which ultimately leads to the ease of synthesis, thereby making them highly desirable material choices in the field of spintronics.

2 Theoretical Framework

This section shall cover the theoretical knowledge required to comprehend the results obtained in the study. We begin by explaining the source and mathematics used in the Density Functional Theory (DFT) used in QE and WIEN2k code. In the following subsection, we shall provide some theoretical background for understanding Heusler alloys.

2.1 Density Functional Theory

DFT is an approach to studying the Schrödinger equation by writing energy in terms of the particle densities instead of the usual wave function. DFT simplifies the computations considerably when solving the many-body problems that are being solved in material simulation.

We are interested in finding the ground state, i.e. the most stable configuration of our many-body system, using the many-body Schrödinger equation. Let us consider an N-atomic system. Its Schrödinger equation is given by :

$$\hat{H}\psi(\{r_i\}, \{R_i\}) = E\psi(\{r_i\}, \{R_i\}) \quad (1)$$

r_i refers to the part of wavefunction due to the electrons, while R_i corresponds to the nuclei. The corresponding Hamiltonian for the many-body system is given by:

$$\hat{H} = \hat{T} + \hat{V}_{ee} \quad (2)$$

where,

$$\hat{V} = \frac{q_i q_j}{|\vec{r}_i - \vec{r}_j|}$$

Corresponds to the electron-electron Coulomb interaction, and \hat{T} corresponds to the kinetic energy term of the wavefunction. We proceed further by simplifying Eq(1) by applying the Born-Oppenheimer approximation, which states that the mass of nuclei is

huge as compared to the mass of electrons and hence, their mechanics can be separated and dealt with individually or in other words assuming that the nuclei and electrons are independent species with nuclei having slow dynamics while electrons having way faster dynamics. We decouple our wavefunction as follows:

$$\psi(\{r_i\}, \{R_i\}) \rightarrow \psi_N(\{R_i\}) * \psi_e(\{r_i\}) \quad (3)$$

This simplifies the calculations since the time needed for electrons to reach their ground state is much faster than when the nuclei dynamics were included. Now, we can focus on the problem with the perspective that the electrons experience some external fixed potential due to the nuclei. This modifies eq(2), and now we only focus on the electronic part of the Hamiltonian :

$$\hat{H} = -\frac{\hbar^2}{2m_e} \sum_i^{N_e} \nabla_i^2 + \sum_i^{N_e} V_{ext}(r_i) + \sum_{i=1}^{N_e} \sum_{j>i} U(r_i, r_j) \quad (4)$$

We proceed by defining the electron density in the following way:

$$n(r) = \psi^*(r_1, r_2, \dots, r_N) \psi(r_1, r_2, \dots, r_N) \quad (5)$$

This modifies our problem, and now, instead of focusing on the individual electron as a wave, we view them as electron density as a whole. It reduces the dimensions significantly from $3N$ previously to only three now.

Our following assumption assumes that any arbitrary j^{th} electron is treated as a point charge inside the field of all other electrons. Hence, our many-electron problem essentially reduces to many one-electron problems which we can solve. By doing this, we can write the Hartree product and redefine our electron density:

$$\begin{aligned} \psi(r_1, r_2, \dots, r_n) &= \psi(r_1) * \psi(r_2) * \dots * \psi(r_3) \\ n(r) &= 2 \sum_i \psi_i^*(r) \psi_i(r) \end{aligned} \quad (6)$$

To proceed further, we have utilized the following two theorems proposed by Hohenberg and Kohn, which bring in the functional part of the Density functional theory and help us express ground state energy in terms of energy.

2.1.1 Hohenberg and Kohn Theorem 1

It states that the ground state energy E can be given as a unique functional of the electron density. A functional is defined as the function of a function; for instance, differentiation $F[f] = \frac{df}{dx}$ is a functional.

$$E = E[n(r)]$$

2.1.2 Hohenberg and Kohn Theorem 2

The second theorem states that the electron density which yields the minimum overall energy of the functional is the true electron density for the system's ground state. To express it mathematically, we can say that any other electron yields a higher energy than the true ground state energy.

$$E[n(r)] > E_o[n_o(r)]$$

where E_o and n_o represent the ground state's true energy functional and electron density, respectively.

Moving on, this energy functional can be broken into two parts, the unknown part known as the exchange-correlation functional and the known part.

$$E[\{\psi_i\}] = E_{known}[\{\psi_i\}] + E_{XC}[\{\psi_i\}]$$

where,

$$E_{known}[\{\psi_i\}] = -\frac{\hbar}{m_e} \sum_i \psi_i^* \nabla^2 \psi_i d^3 r + \int V(r) n(r) d^3 r + \frac{e^2}{2} \iint \frac{n(r) - n(r')}{r - r'} d^3 r d^3 r' + E_{ion} \quad (7)$$

The following terms are the electron's kinetic energy, the interaction between nuclei and an electron, the interaction term between two electrons, and the interaction term between two nuclei.

The remaining exchange-correlation functional $E_{XC}[\{\psi_i\}]$ incorporates all the necessary quantum mechanical terms which account for the electron-electron interactions for the system and need to be estimated as it is unknown. Various correlation functionals, as shown in Fig(1), already constructed, work well with the experimental results. Still, the quest is yet to find an accurate correlation functional, which is also computationally effective.

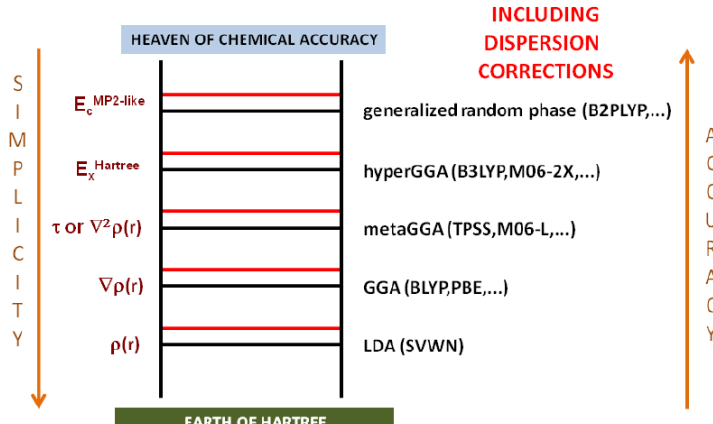


FIGURE 1: *Jacob's Ladder*[9]

As we climb up the Jacob's ladder (Fig[1]), we achieve higher accuracy at the cost of computation. The functionals, including meta-generalized gradient approximation (GGA) and above, include the orbital interactions in the systems, which typically offer better accuracy. The most commonly used correlation functional for solids is GGA, which offers better accuracy over the primitive Local Density Approximation (LDA). HyperGGA is available as a hybrid functional in various software and is considered the most advanced and accurate, but it is pretty computationally intensive.

2.1.3 Kohn-Sham scheme

Now that we have set the energy as functionals of the electron density, we write and solve the Hamiltonian for a set of single electron wave functions, which only depend on three spatial variables, $\psi(r)$.

$$\left[-\frac{\hbar^2}{2m} \nabla^2 + V(r) + V_H(r) + V_{XC}(r) \right] \psi_i(r) = \epsilon_i(r) \psi_i(r) \quad (8)$$

The following terms in Eq(8) correspond to the kinetic energy of the electron, potential due to the nucleus, potential due to the electron density, i.e. due to other electrons and the exchange potential, respectively. We employ the self-consistent scheme to solve these multiple Kohn-Sham equations self-consistently, starting with an initial guess for the electron density. Hence, this is also called the self-consistent frequency (SCF) cycle.

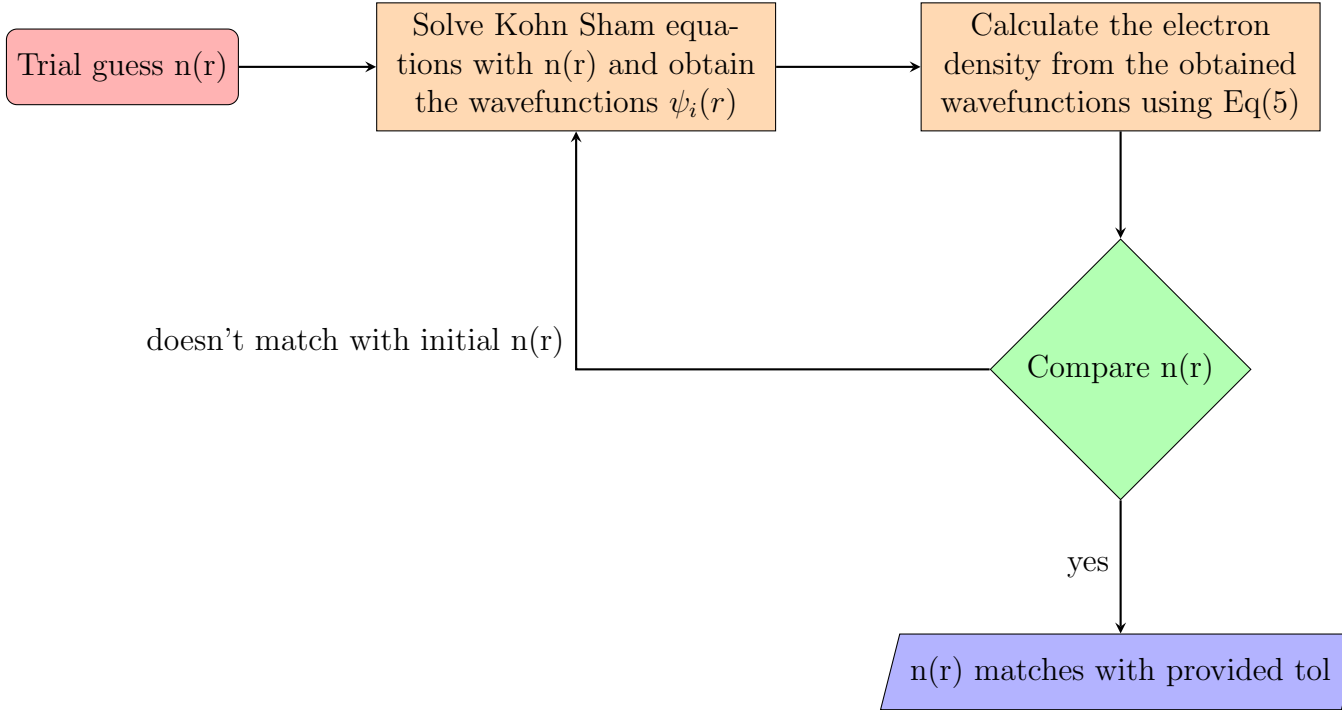


FIGURE 2: *Flow chart for the SCF calculation*

Once we obtain the electronic ground state, we can proceed with calculating the ionic forces on atoms, which is straightforward as below:

$$F_i = -\frac{dE}{dr_i} = - \left\langle \psi_i \left| \frac{\partial \hat{H}}{\partial r_i} \right| \psi_i \right\rangle \quad (9)$$

We can move along the ionic forces to obtain the corresponding ionic ground state, which is done during the relaxation calculation. Once this is achieved, we can calculate many other properties by displacing the ions from the ground state and determining forces on other ions. It helps us calculate the system's force constants and vibrational frequencies, such as the phonon dispersion frequencies.

2.1.4 Plane Wave DFT

To apply DFT to crystalline solids, we consider the free electrons as plane waves, and the crystals are nothing but a repetition of ions or periodic potential, say some $U(r)$. Hence, the electrons in a periodic potential are known as Bloch waves, which gives us the perturbed free electrons in the lattice given by:

$$\psi_{nk}(r) = \exp(ikr)U_{nk}(r) \quad (10)$$

Reciprocal Lattice

We use the concept of reciprocal lattice, which is nothing but a Fourier transformation of the Bloch waves. A reciprocal lattice is a mathematical construct to describe wave

vectors and analyze crystals. Since all periodic functions can be expanded as a Fourier Series, we expand Eq(10)

$$\psi_{nk} = \exp(ikr) \sum_G c_k \exp(iGr) \quad (11)$$

Hence, the Bloch waves can be represented as a sum of plane waves, with a wave vector defined as $G+k$ with kinetic energies, $E = \frac{\hbar^2}{2m}|k + G|^2$. Since the series summation is infinite, we have to define a cutoff energy for this summation, chosen after testing for convergence in the calculations, which is an essential parameter while performing calculations.

Brillouin Zone

Another critical concept in DFT is the Brillouin zone (BZ). A primitive unit cell in the reciprocal space is called a Brillouin zone. Any lattice vectors which differ by a reciprocal lattice vector G are equivalent due to the repetitiveness of the lattice, i.e., $k' = k + G$. All integrals calculated in the DFT are done for the 1st BZ.

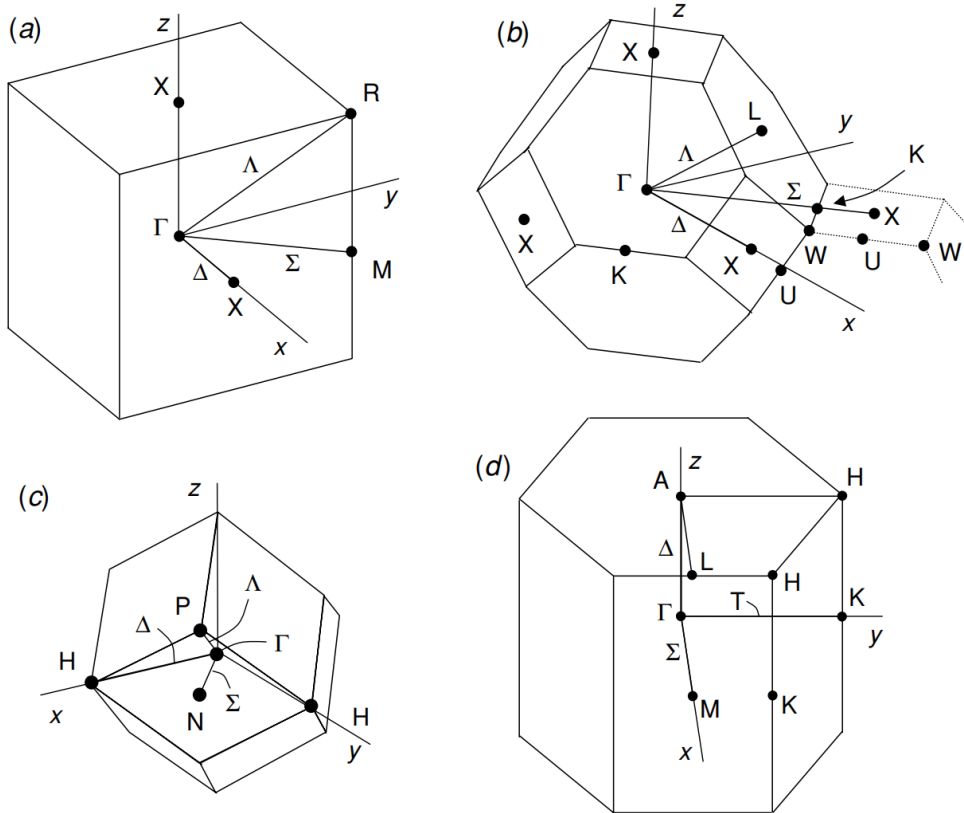


FIGURE 3: Brillouin Zones for (a) simple cubic (SC), (b) face centered cubic (fcc), (c) body centered cubic (bcc), (d) hexagonal (hex)[10]

To solve the systems in these BZ, we must choose an appropriate number of K-points to sample the BZ. These K-points are sampled with respect to energy convergence.

2.2 Heusler Alloys

Heusler alloys are a fascinating class of intermetallic compounds known for their diverse magnetic and electronic properties. They make them suitable for spintronics, thermoelectrics, and magnetic refrigeration applications. Named after the German chemist Friedrich Heusler, who first discovered them, these alloys typically have compositions represented as X_2YZ or XYZ , where X and Y are transition metals, and Z is a main group element.

Heusler alloys can be broadly classified into three main types:

2.2.1 Regular Heusler Alloys

These alloys have the stoichiometry X_2YZ and crystallize in the cubic L₂1 structure, characterized by the space group $Fm\bar{3}m$. In this structure, the X atoms occupy two distinct Wyckoff positions, forming a face-centered cubic lattice with Y and Z atoms occupying alternate faces. This arrangement leads to a highly ordered structure. Full Heusler alloys are known for their high degree of spin polarization and are of particular interest in spintronic devices.

2.2.2 Half-Heusler Alloys

With the formula XYZ , these alloys adopt the C1_b structure, essentially a three-quarters filled version of the L₂1 structure with one of the X sites vacant. This results in a non-centrosymmetric space group $F\bar{4}3m$. Half-Heusler alloys have been studied extensively for their thermoelectric properties and topological insulator behaviour.

2.2.3 Inverse Heusler Alloys

Inverse Heusler alloys also have the composition X_2YZ but differ in their atomic arrangement. They crystallize in the inverse Heusler structure with space group $F\bar{4}3m$, similar to the half-Heusler structure but fully occupied. In this structure, the distribution of X and Y atoms differs from that of regular Heusler alloys, leading to different electronic and magnetic properties.

2.2.4 Properties and Applications

Heusler alloys exhibit various magnetic properties, from ferromagnetic to antiferromagnetic, depending on the nature of the transition metals used and their electronic configurations. The flexibility in their composition allows for the tuning of electronic properties, making them highly adaptable for various applications. For instance:

- Spintrronics: Due to their high spin polarization, Heusler alloys are ideal candidates for spintronic applications, where electronic devices operate based on the spin of electrons rather than their charge.
- Thermoelectrics: Half-Heusler alloys are particularly noted for their high thermoelectric efficiency, which makes them suitable for converting waste heat into electricity.
- Magnetic Refrigeration: Some Heusler alloys undergo magnetocaloric effects, which are helpful in magnetic refrigeration technology, an energy-efficient cooling technology.

2.2.5 Challenges and Innovations

Despite their potential, challenges such as achieving high spin polarization in practical devices and optimizing thermoelectric properties at room temperature remain. Ongoing research aims to address these issues through alloying, treatment processes, and nanosstructuring, which have shown promise in enhancing the desirable properties of Heusler alloys.

In summary, Heusler alloys represent a versatile and promising field in materials science, offering many opportunities for fundamental research and technological applications. Their structural diversity and tunable properties make them a focus of intense research aimed at new and improved materials for future technologies.

3 Softwares

3.1 WIEN2k

The Full Potential Linearized Augmented Plane Wave + local orbitals (FP-LAPW+lo) method has proven to be one of the most accurate methods for computing the electronic structure of solids within density functional theory. The first copyrighted version was WIEN, published by P. Blaha, K. Schwarz, P. Sorantin, and S. B. Trickey in *Comput. Phys. Commun.* 59, 399 (1990).

WIEN2k is written in FORTRAN 90 and requires a UNIX/Linux-type operating system since the programs are linked via C-shell scripts. Hardware requirements will change from case to case, but small cases with 60 atoms per unit cell can be run on any Intel (AMD) based PC/Laptop. One of its distinguishing features is the ability to handle complex structures, including those with lower symmetry or large unit cells, making it particularly powerful for studying a wide variety of materials. The software supports various exchange-correlation functionals, including local density approximation (LDA), generalized gradient approximation (GGA), and more advanced functionals like meta-GGA and hybrid functionals. This versatility enables users to tailor their calculations to specific requirements and achieve reliable results.

3.1.1 FP-LAPW

The LAPW method has proven to be one of the most accurate methods for computing the electronic structure of solids within density functional theory. The LAPW method is a procedure for solving the Kohn-Sham equations for the ground state density, total energy, and (Kohn-Sham) eigenvalues (energy bands) of a many-electron system (here, a crystal) by familiarising a basis set which is specially adapted to the problem.

The unit cell is divided into two parts: the atomic sphere, which is non-overlapping, and the interstitial region between them. In both regions, different basis sets are used to solve the Kohn-Sham equation. For in-depth details of the LAPW method, we can refer to a book by Singh and Nordström [11].

- Inside the sphere:

$$\phi_{k_n} = \sum_{lm} [A_{lm,k_n} u_l(r, E_l) + B_{lm,k_n} \dot{u}_l(r, E_l)] Y_{lm}(\hat{r}) \quad (12)$$

where $u_l(r, E_l)$ is the regular solution of the radial Schrödinger equation for energy E_l and the spherical part inside the sphere. $\dot{u}_l(r, E_l)$ is the energy derivative of u_l .

A_{lm} and B_{lm} depend on k_n . A linear combination of these two gives the Linearization of the radial function. u_l and \dot{u}_l can be obtained by numerical integration of Schrödinger equation on a radial k-mesh inside the sphere.

- Inside the interstitial region:

$$\phi_{k_n} = \frac{1}{\sqrt{\omega}} \exp ik_n r \quad (13)$$

$k_n = k + K_n$ are the reciprocal lattice vectors, and k is the wave vector inside the first BZ. Each plane wave is augmented in an atomic-like function in every atomic sphere.

The solutions to Kohn-Sham equations derived in Eq(10) are expanded in this combined basis set of LAPW's.

$$\psi_{kn} = \sum_n c_n \phi_{k_n} \quad (14)$$

The convergence of this basis set is controlled by a cutoff parameter $RMT \times K_{max} = 6 - 9$, where RMT is the smallest atomic sphere radius in the unit cell and K_{max} is the magnitude of the largest K vector in the Eq(14).

3.1.2 APW+lo

Improvements were made in the FP-LAPW approach by improving the Linearization and enabling a consistent treatment of semi-core and valence states in one energy window. Additional basis functions were added independent of k_n and called local orbitals (LO) to achieve this.

$$\phi_{lm}^{lo} = [A_{lm}u_l(r, E_{1,l}) + B_{lm}\dot{u}_l(r, E_{1,l})Y_{lm}(\hat{r})] \quad (15)$$

Eq(15) appears similar to eq(14), but here, A_{lm} and B_{lm} do not depend on k_n and are determined by the condition that the LO is zero at the sphere boundary and normalized. Note that the total wave function is still smooth and differentiable. As shown in the reference [12], this new scheme converges practically to identical results as the LAPW method. Still, it allows the reduction of RK_{max} by about one, leading to significantly smaller basis sets (up to 50%). Thus, the corresponding computational time is drastically reduced (up to an order of magnitude).

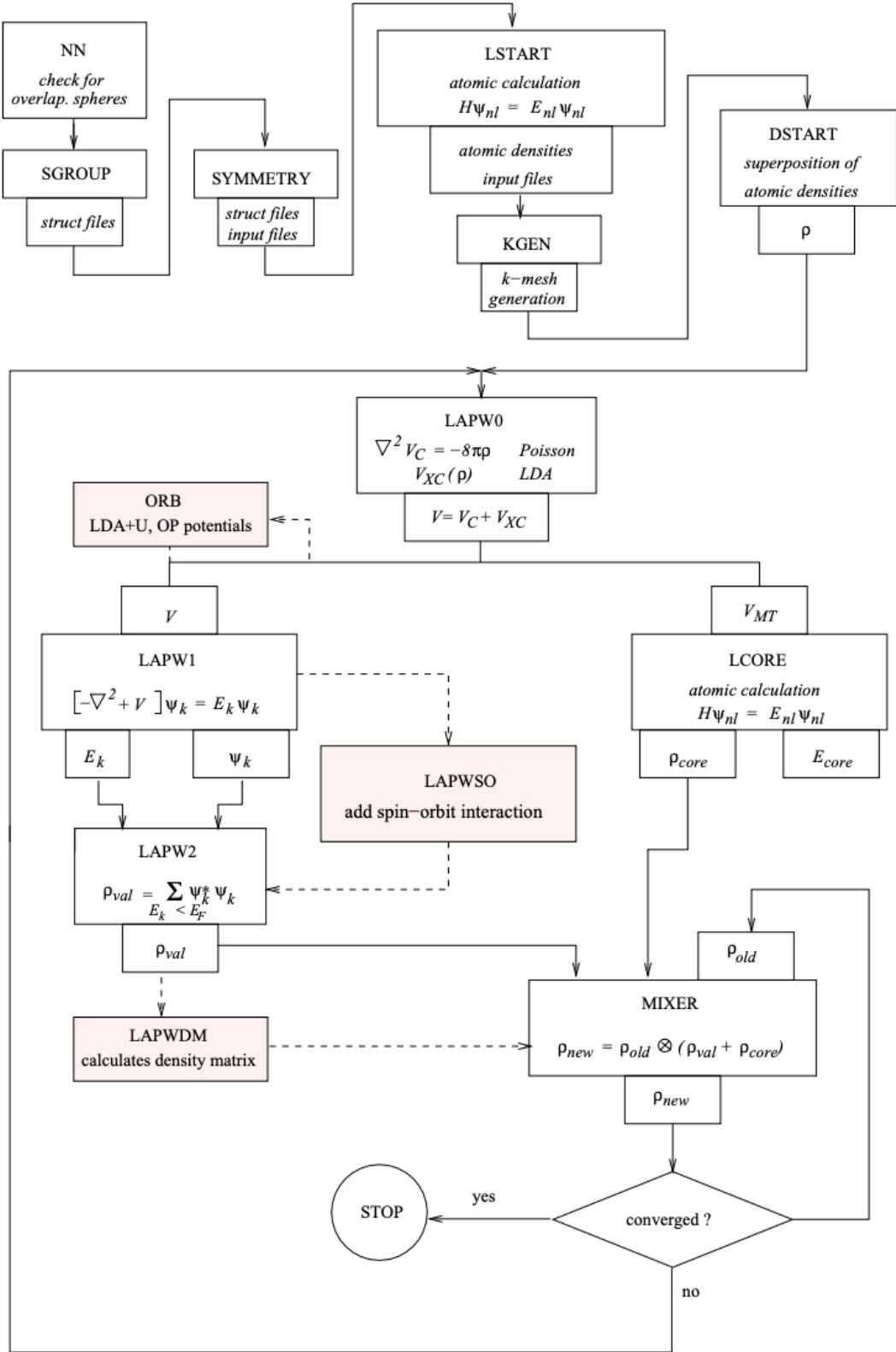


FIGURE 4: Program flow in WIEN2k[13]

3.2 Quantum Espresso

Quantum ESPRESSO (QE) is an advanced computational chemistry software suite designed primarily for simulations of electronic structure properties of materials using DFT, plane waves, and pseudopotentials. This software is widely recognized in materials science for its robust capabilities in providing accurate, high-precision calculations of the electronic properties and total energy of bulk and reduced-dimensional systems.

QE stands out for its modular design, allowing researchers to perform various calculations, including structural optimization, molecular dynamics simulations, and electronic and magnetic properties studies. The suite supports multiple types of DFT functionals. It incorporates corrections such as van der Waals interactions and Hubbard U, enhancing its versatility and applicability to various material types. It is particularly noted for its ability to handle periodic three-dimensional, two-dimensional, one-dimensional, and zero-dimensional systems.

The efficiency of QE is driven by its use of plane waves as the basis for electronic calculations, combined with pseudopotentials to simplify the treatment of electron-ion interactions. This combination enables the simulation of complex materials systems with considerable accuracy while being computationally efficient. The software is also designed for high-performance computing environments and can run on large parallel clusters, which is crucial for tackling computationally demanding tasks.

3.2.1 Pseudopotentials

Pseudopotentials simplify the treatment of electron-ion interactions by explicitly removing the need to consider core electrons in the calculations. They represent an effective potential seen by the valence electrons, capturing the effect of the atomic core on them without involving actual core electron states. The choice of pseudopotentials is pivotal because it affects calculations' accuracy, efficiency, and convergence.

3.3 VESTA

VESTA is a versatile and powerful software package for visualizing and analyzing crystal structures and electron/nuclear densities in three dimensions. It is widely used by researchers in crystallography, materials science, and chemistry for its robust visualization capabilities and user-friendly interface.

- **Visualization:** VESTA excels in creating detailed, high-quality visual representations of crystal structures, molecular structures, and 3D data such as charge densities and potential maps. It supports multiple visualization modes, including ball-and-stick, space-filling models, and polyhedral.
- **Data Analysis:** Beyond visualization, VESTA provides tools for analyzing structural parameters such as bond lengths, angles, and other geometrical data. It also allows for the simulation of X-ray and neutron powder diffraction patterns, which is essential for comparing theoretical models with experimental data.
- **File compatibility:** VESTA supports various file formats used in computational chemistry and materials science, making it highly versatile and compatible with other software tools.

4 Methodology

4.1 Implementation

This section will cover the input files or the initialization for WIEN2k and QE.

4.1.1 WIEN2k

Structure File

The first and foremost task in WIEN2k is to create a .struct file for your system. This can be done via the interactive graphical user interface (GUI) w2web, or a Crystallographic information file (CIF) can be imported from software like VESTA. While working in WIEN2k, we must ensure that the struct file matches the name of the folder we are working in.

Initialization

Next, we proceed with the initialization for the SCF calculation by running the init_lapw script. This initialization has many flags that we can set according to our calculation. Some of the flags I used frequently are listed below:

- -h: Help flag for the script
- -b: batch mode, i.e., default parameters
- -sp: Initializing for spin-polarized calculation
- -red: Reduction in % for the muffin tin radius (RMT)
- -ecut: Energy separation value between the core and valence electrons
- -rkmax: Value for RK_{max}
- -lmax: Value for L_{max}
- -gmax: Value for G_{max}
- -numk: Specifies the number of k-points in the 1st BZ

Values of RK_{max} , K-points, and ecut affect our calculation heavily and must be chosen after converging with respect to energy, as shown in section 4.2.

Moving on, we are now ready to perform the SCF calculation for our system using the runsp_lapw (for spin-polarized calculation) or run_lapw (for non-spin-polarized calculation) script included in the WIEN2k package. This script must be run in the working directory. Flags for these scripts can be referred to in the WIEN2k userguide[13].

Further, we used WIEN2k to perform volume optimization and implement PBE, mBJ, and YS-PBE0(similar to hybrid functional HSE06 [14]), potential for calculation of band-structure and density of states (DOS).

Volume Optimization

The program "optimize" (x optimize) generates a series of struct files based on our input with various volumes. It also produces a shell-script optimize.job, similar to Fig ??.

```
#!/bin/csh -f
foreach i ( \
    tic_vol_-10.0 \
    tic_vol_-5.0 \
    tic_vol_0.0 \
    tic_vol_5.0 \
    tic_vol_10.0 \
)
    cp $i.struct tic.struct
#    cp $i.clmsum tic.clmsum
#    x dstart
#    run_lapw -ec 0.0001 -in1new 3 -renorm
run_lapw -ec 0.0001
set stat = $status
if ($stat) then
    echo "ERROR status in" $i
    exit 1
endif
save_lapw ${i}
#    save_lapw -f -d xxx $i
end
```

FIGURE 5: *optimize.job*[13]

We can modify this script to our needs, for instance, exchanging the run_lapw with runsp_lapw. Next, we can use the eplot_lapw script to plot the volume V/S energy curve or lattice parameter V/S energy curve. Alternatively, we can also use Python, Gnuplot or Origin to plot these curves after running the grepline script, which will give us a summary of total energy V/S Volume.

Density of States

DOS is plotted by first preparing a denser k-mesh for DOS calculation using x kgen. Next, we run "x lapw1 -up" and "x lapw1 -dn", which generates eigenvalues and eigenvectors according to the denser k-mesh. Then, we run "x lapw2 -qtl -up" and "x lapw2 -qtl -dn", which generate valence charge density expansions([13]) for up and down spin, respectively. Finally, appropriate DOS is generated using "x tetra -up" and "x tetra -dn", which creates .dosevup and .dosevdn files for the DOS data.

Bandstructure

To plot the band structure, we first need the K-map for the system we are plotting to plot the band structure. This can be done by getting it from the Bilbao Cryst Server or using XCrysden according to our lattice type. Again, we run the "x lapw1" and "x lapw2" commands similarly to DOS for the k-map. Finally, "x spaghetti -up" and "x spaghetti -dn" are run to calculate the band structures, which generate the .agr file containing the information about the bands. This can be plotted in any plotting software or via the w2web GUI.

mBJ potential

Implementing mBJ potential begins once normal initialization is completed. We run the "init_mbj_lapw" script, which creates case.inm.tau file and sets "R2V" in case.in0 file.

Next, we run a single iteration of SCF using "runsp_lapw -i 1" and run "init_mbj_lapw" again. The second run allows us to select parameters of the original mBJ potential. Once this is completed, whenever we use the command "run(sp)_lapw", it will run with the mBJ potential. A common error while running mBJ occurred when the RMT reduction was set to zero; RMT reduction must be at least 5% for mBJ potential.

HSE potential

Initialization for hybrid potential is similar to that of mBJ(4.1.1). First, we let one entire cycle of SCF get completed to get information about the filled and empty bands. We save this cycle by "save_lapw -d pbe", which saves the PBE run in a pbe directory. Next, we run "init_hf_lapw", which creates a case.inhf file. We edit the number of bands (nband) in this file to be at least one greater than the last occupied band as obtained from the SCF calculation. We then provide a reduced k-list since the hybrid calculation is computationally expensive; we must do it on a reduced k-mesh. Next, we run the SCF with HSE potential by adding the "-redklist" flag in the "run(sp)_lapw" command.

4.1.2 Quantum Espresso

Input file

```

&control
  calculation = 'scf'
  prefix = 'Fe2ScSi'
  pseudo_dir = '/home/physicslab/Documents/pseudo/'
  outdir = './'
  verbosity = 'high'
  wf_collect = .true.
/

&system
  ibrav = 2
  celldm(1) = 11.0733
  nat = 4
  ntyp = 3
  ecutwfc = 90
  ecutrho = 720
  nspin = 2
  starting_magnetization(1) = 0.5
  starting_magnetization(2) = 0.5
  starting_magnetization(3) = 0.5
  occupations = 'smearing'
  smearing = 'gaussian'
  degauss = 0.05
/
&electrons
  mixing_mode = 'plain'
  mixing_beta = 0.7
  conv_thr = 1.0e-8
/
ATOMIC_SPECIES
  Fe 55.845  Fe,pbe-spn-rrkjus_psl.1.0.0.UPF
  Sc 44.955912 Sc,pbe-spn-rrkjus_psl.1.0.0.UPF
  Si 28.0855  Si,pbe-nl-rrkjus_psl.1.0.0.UPF
ATOMIC_POSITIONS
  Sc 0.00 0.00 0.00
  Fe 0.25 0.25 0.25
  Fe 0.75 0.75 0.75
  Si 0.50 0.50 0.50
K_POINTS {automatic}
  8 8 8 0 0 0

```

FIGURE 6: *Input file for SCF in QE*

Some of the important flags used in the QE input file (Fig 6) for SCF are given below:

- calculation: Specifies the calculation to be performed.
- prefix: This defines your calculation. All calculations in QE must be done under the same prefix.
- pseudo_dir: This flag defines the path where the pseudopotential has been downloaded on your system.
- outdir: Defines the path where the output files must be stored.
- verbosity: Decides how much information will be printed in the output file.
- ibrav: Stands for the lattice type. 2 stands for FCC lattice.
- celldm: Defines the lattice parameter.
- nat: Number of atoms in the unit cell.
- ntyp: number of types of atom.
- ecutwfc: Kinetic energy cutoff (Ry) for the wavefunctions.
- ecutrho: Kinetic energy cutoff (Ry) for charge density and potential.
- nspin: Specifies the spin-polarized calculation.
- starting_magnetization: Initial guess for the code to begin the SCF cycle.
- occupations: Specifies how the electronic states are occupied in calculations, particularly relevant in systems with partial occupancy of electronic states, such as metals.
- ATOMIC_POSITIONS: specifies the positions in the unit cell.
- K_POINTS: Specifies the number of K-points used in the k-mesh.

SCF calculation is run via the terminal using the command "pw.x *scf.in*; scf.out" via the pw.x package and "mpirun -np 8 pw.x *scf.in*; scf.out" in case the QE is installed for parallel execution. Mpirun runs the calculation across multiple CPU cores specified by the -np flag.

Phonon

To calculate the phonon frequency plot and the phonon dispersion curves, we must first perform a SCF calculation 4.1.2. Then, we prepare an input file for the package "ph.x", which calculates a dynamical matrix on uniform q points. This calculation is computationally expensive and must first be done on fewer q-points. Next, we perform an inverse Fourier transform of the dynamical matrix to obtain inverse Fourier components in real space using "q2r.x". Finally, we perform the Fourier transformation of the real space components to get the dynamical matrix at any q using matdyn.x.

Elastic properties

Elastic constants were calculated in QE using the "thermos_pw.x" package. Implementation is relatively straightforward for calculating elastic properties; we first create the input file for SCF. We also write a thermos_control file, which is necessary for the thermos_pw package. Using the elastic constants tensor, the code can calculate and print a few auxiliary quantities: the bulk modulus, the poly-crystalline averages of the Young modulus, the shear modulus, and the Poisson ratio. The Voigt and the Reuss averages are printed together with the Hill average. The Voigt-Reuss-Hill average of the shear and bulk modulus are used to compute average sound velocities. The average of the Poisson ratio and the bulk modulus allows the estimation of the Debye temperature. The Debye temperature is also calculated using the exact formula evaluating the average sound velocity from the angular average of the sound velocities calculated for each propagation direction, solving the Christoffel wave equation. The exact Debye temperature is used within the Debye model to calculate Debye's vibrational energy, free energy, entropy, and constant strain heat capacity. These quantities are plotted in a postscript file as a function of temperature.

4.2 Optimizations

4.2.1 WIEN2k

Optimization of parameters was carried out for Fe₂ScSn, and its results were used to perform further calculations for all systems due to the similar nature of all three Heusler alloys.

E cut

The -ecut parameter was defined as the energy separation value between the core and valence electrons in section 4.1.1. Multiple SCF runs were performed while keeping all other parameters constant and varying the -ecut in the specified range according to WIEN2k[13].

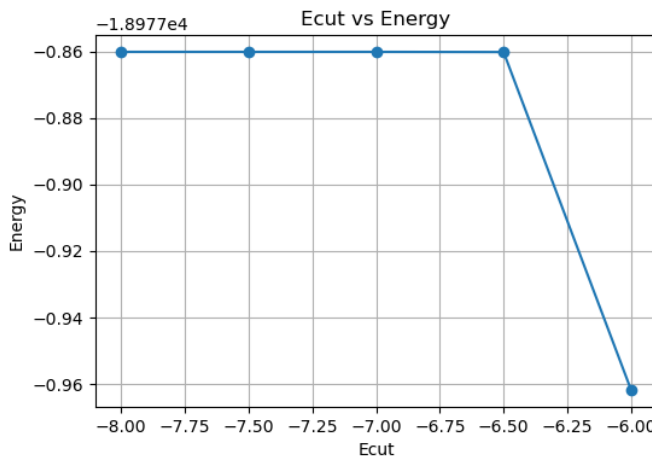


FIGURE 7: Optimization plot for ecut parameter in WIEN2k

We observe a sharp minimization in total energy after -6Ry; hence the -ecut parameter was set to -6Ry.

RK_{max}

A similar optimization was performed for -rkmax, which is defined as the maximum value of the product of the smallest atomic sphere and largest wave vector.

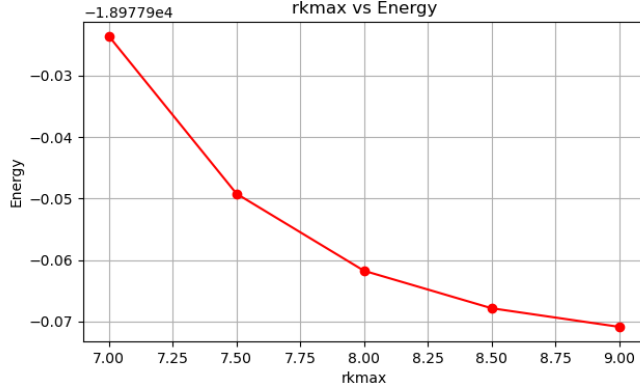


FIGURE 8: Optimization plot for RKmax parameter in WIEN2k

The -rkmax parameter successfully displayed converging behaviour up to 4 places of decimal. Increasing -rkmax greatly influences the computation cost and hence, a value of 8 was chosen after analyzing the results.

R_MT reduction

Finally, a convergence test was performed for the -red parameter, which defines the percentage reduction in the RMT radius of atoms.

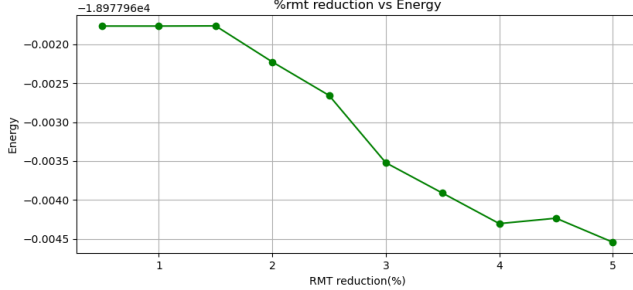


FIGURE 9: Optimization plot for RMT reduction parameter in WIEN2k

The RMT reduction parameter displayed a gradual minimization in energy in the fourth decimal place; hence, it does not affect the calculation significantly in our case. A value of 5% reduction was chosen to adjust for volume optimizations and apply different potentials.

4.2.2 Quantum ESPRESSO

Similar optimization was carried out for Fe₂ScSi for parameters in QE to test for convergence.

E cut

The kinetic energy threshold value for wavefunctions was varied, and multiple runs were performed to test for the convergence.

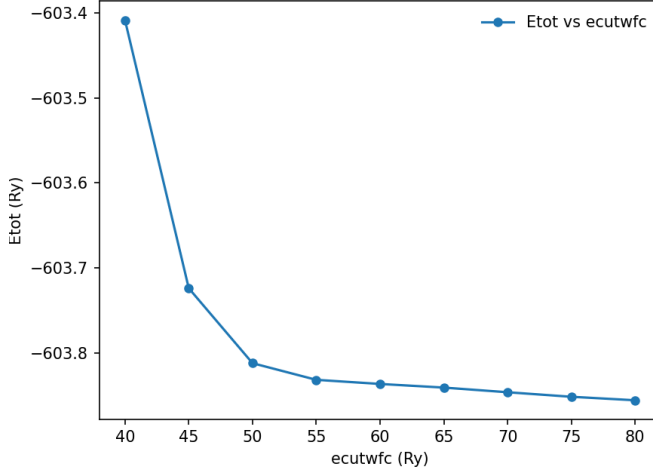


FIGURE 10: Optimization plot for *ecut* parameter in *QE*

A good convergence was achieved in the *ecutwfc* parameter. Like WIEN2k, the *ecut* parameter significantly affects the computational cost, so a value of 80 Ry was chosen.

K points

The number of k-points determines the points in the 1st BZ over which integrations will be carried out. A denser k-mesh leads to accurate results but more computation cost. A convergence test was performed for the number of k-points.

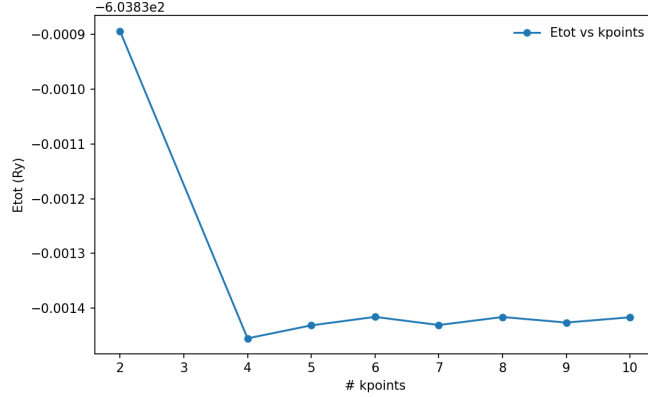


FIGURE 11: Optimization plot for *K* points in *QE*

K-points converged up to 4 places of decimals, and a value of $8 \times 8 \times 8$ was chosen for a dense enough k-mesh.

4.3 Computational Detail

4.3.1 WIEN2k

The plane-wave cutoff parameter was taken as $RMT \times K_{max} = 8$ to determine the matrix size, where RMT is the smallest muffin-tin (MT) sphere radius, and K_{max} is the maximum modulus of reciprocal lattice vectors $K = k + G$ in the first BZ. The maximum partial wave value inside the muffin tin sphere was set as $l_{max} = 10$. We expanded the potential and the charge density as a Fourier series with wave vectors up to $G_{max} = 12a.u^{-1}$. The cutoff energy separating the valence and core states was chosen to be $-6Ry$. Integrations in the irreducible first BZ were performed using 49 special k points based on a mesh of size $10 \times 10 \times 10$. The (SCF) iteration process was terminated when the change in the absolute value of the total energy was less than $10^{-4}Ry$. For hybrid potential calculation, a reduced Q-mesh was considered for $1 \times 1 \times 1$ along with k -mesh of $6 \times 6 \times 6$ due to the computationally expensive calculation.

4.3.2 Quantum ESPRESSO

The wave functions were expanded in a plane-wave basis set with a kinetic energy cutoff of $ecutwfc = 90$ Ry. Brillouin-zone integrations were performed using a $8 \times 8 \times 8$ k -point mesh. Integration up to the Fermi surface was performed using the Gaussian smearing technique with a smearing parameter $degauss = 0.05$ Ry. The SCF iteration process was terminated when the change in total energy was less than $conv_thr = 1.0e - 8$. Further phonon calculations were performed on q-mesh of $2 \times 2 \times 2$.

5 Results

5.1 Structure

The study of two different site coordination structural inverse types and regular types for Fe_2ScZ ($Z=Si; Ge; Sn$). For inverse structure, the F.C.C structure of the bulk Fe_2ScZ is in the $F\bar{4}3m$ space group with the coordinates of $(0,0,0)$, $(0.25,0.25,0.25)$ for Fe, $(0.5,0.5,0.5)$ for Sc, and $(0.75,0.75,0.75)$ for Si/Ge/Sn atoms as portrayed in Fig 12,13,14.

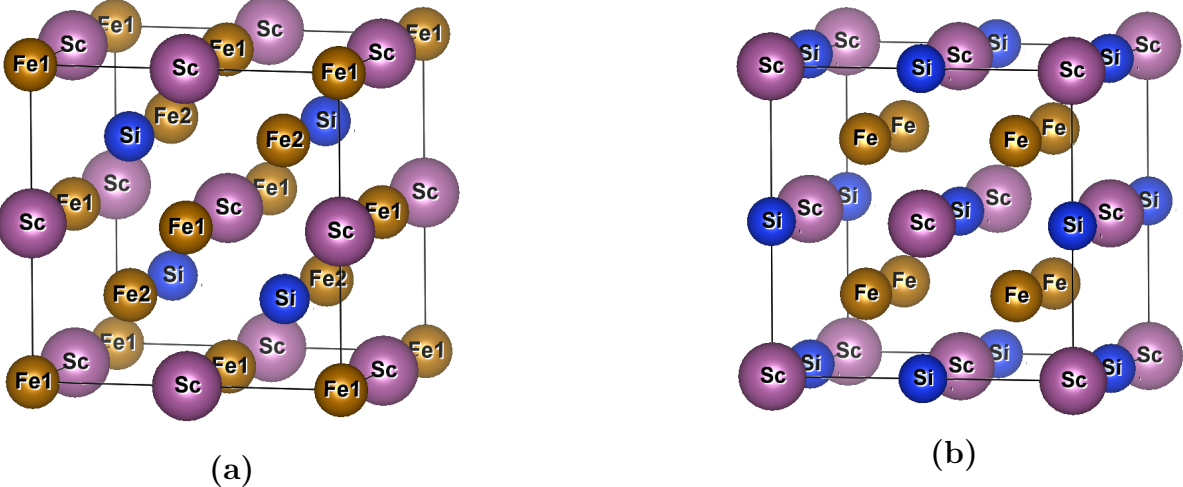


FIGURE 12: (a) Inverse structure of Fe_2ScSi (b) Regular structure of Fe_2ScSi

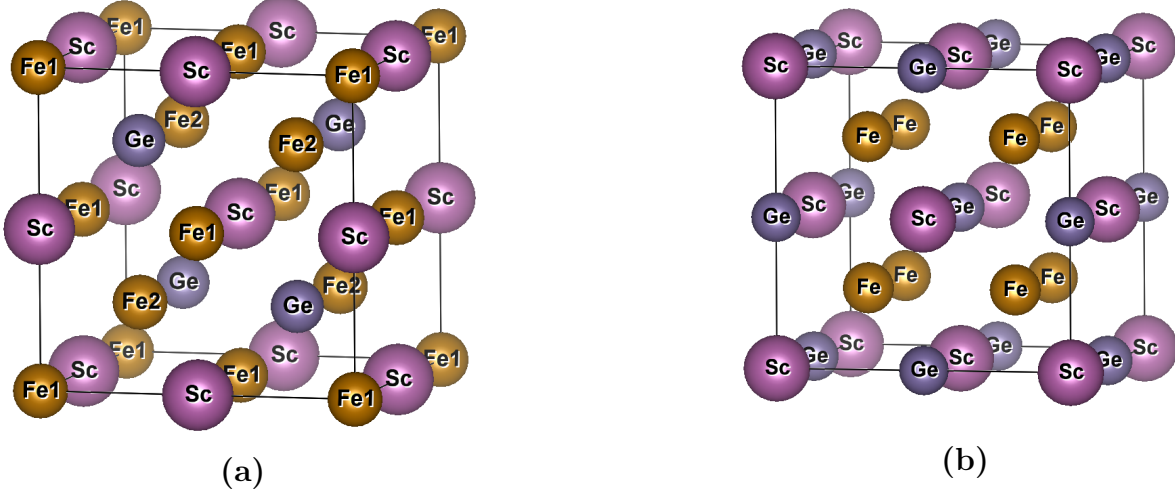


FIGURE 13: (a) Inverse structure of Fe_2ScGe (b) Regular structure of Fe_2ScGe

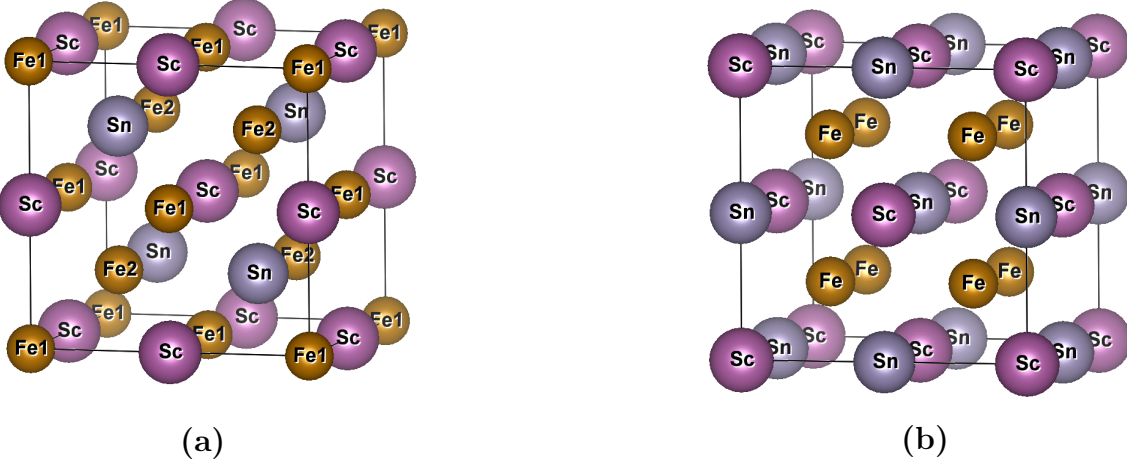


FIGURE 14: (a) Inverse structure of Fe_2ScSn (b) Regular structure of Fe_2ScSn

On the contrary, for regular Heusler, the structure is in the $Fm\bar{3}m$ space group with the coordinates of (0.25,0.25,0.25), (0.75,0.75,0.75) for Fe, (0,0,0) for Sc, and (0.5,0.5,0.5) for Si/Ge/Sn as portrayed in Fig 12,13,14.

The first step is to obtain the ground state point with its equilibrium volume to find accurate results. The total change in energy of Fe_2ScZ versus its unit cell volume ($E-V$) and fit with the Birch-Murnaghan equation of state[15]:

$$E(V) = E_0 + \frac{9B_0V_0}{16} \left[B' \left[\left(\frac{V_o}{V} \right)^{\frac{2}{3}} - 1 \right]^3 + \left[\left(\frac{V_0}{V} \right)^{\frac{2}{3}} - 1 \right]^2 \left[6 - 4 \left(\frac{V_0}{V} \right)^{\frac{2}{3}} \right] \right] \quad (16)$$

B_0 and B' are the bulk moduli and the first pressure-derivative, respectively. The volume-dependent pressure P , bulk modulus B are given by: $P = -\frac{dE}{dV}$; $B = -V \frac{dP}{dV} = V \frac{d^2E}{dV^2}$; $B' = \frac{dB}{dP}$. The diagram is shown in Fig (15,16) in the ferromagnetic (FM) and non-magnetic (NM) phases for both regular and inverse structures.

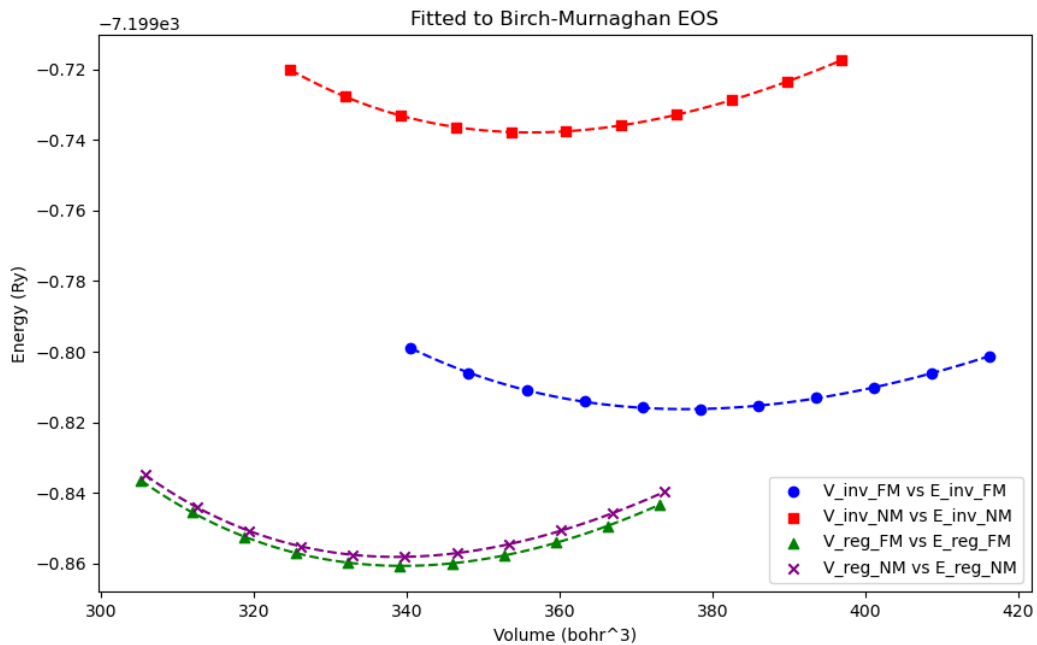


FIGURE 15: *Volume optimization plot for Fe_2ScSi*

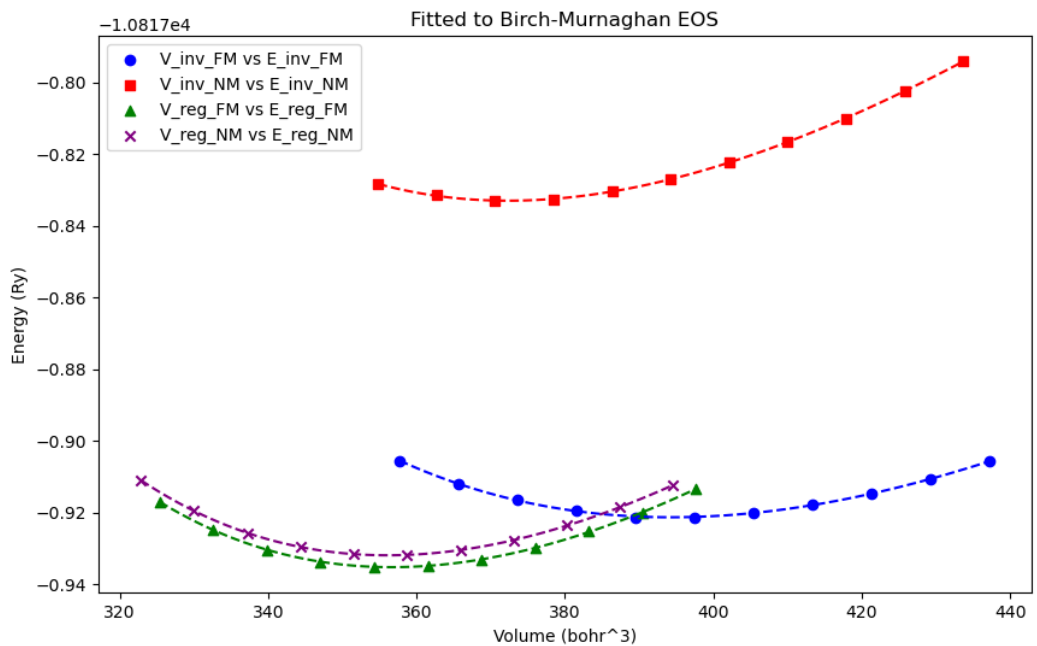


FIGURE 16: *Volume optimization plot for Fe_2ScGe*

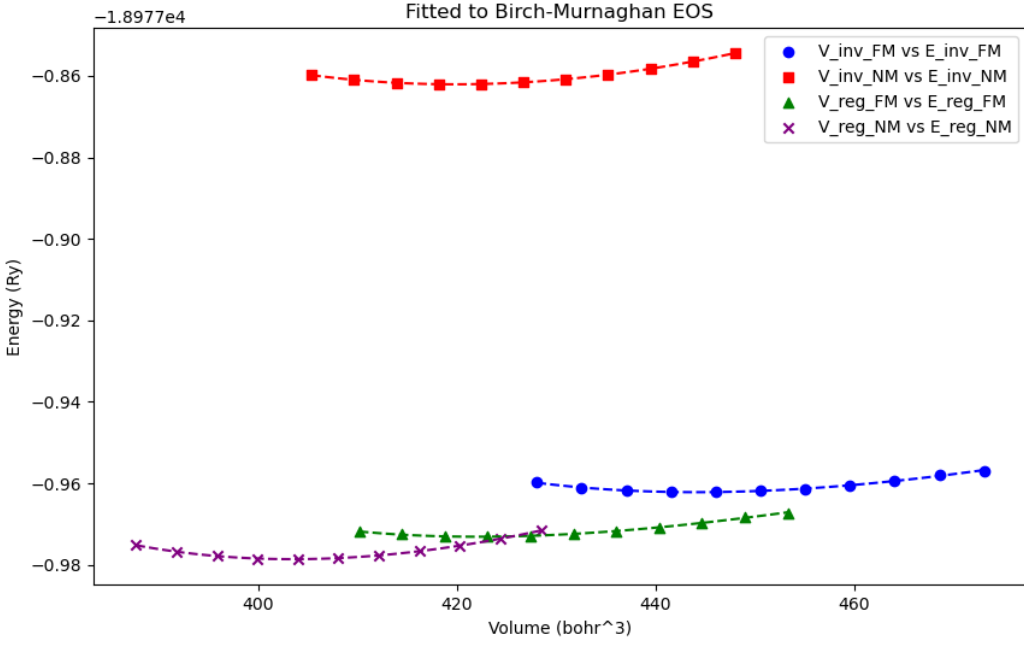


FIGURE 17: *Volume optimization plot for Fe_2ScSn*

Alloy	Type	M. State	a (\AA)	V (\AA^3)	$E_0(Ry)$	$\mu_b(\text{BM})$	B (GPa)	B'
Fe_2ScSi	Regular	NM	11.0645	338.6401	-7199.85811		177.9717	4.4428
		FM	11.0733	339.4433	-7199.86065	0.93716	176.0971	3.5337
	Inverse	NM	11.2526	356.2061	-7199.737924		158.274	4.619
		FM	11.4620	376.4620	-7199.816264	4.66148	124.6479	4.1473
Fe_2ScGe	Regular	NM	11.2510	356.0507	-10817.93193		166.6309	4.4477
		FM	11.2571	356.6318	-10817.93524	2.60759	165.9459	4.4513
	Inverse	NM	11.4196	372.3016	-10817.83301		152.6496	4.9268
		FM	11.6397	394.2454	-10817.92132	4.76	116.9207	4.0045
Fe_2ScSn	Regular	NM	11.7291	403.4027	-18977.97861		151.0243	5.3994
		FM	11.9072	422.0532	-18977.9731	3.13889	99.8736	10.1465
	Inverse	NM	11.8855	419.7562	-18977.86208		129.026	2.976
		FM	12.1084	443.8167	-18977.96221	4.7255	108.9809	11.7789

TABLE 1: *Calculated properties for Fe_2ScSi , Fe_2ScGe , and Fe_2ScSn alloys*

As we can observe from Table 1, the regular Heusler structures are more stable than the inverse structure. Hence, all the calculations in the further sections are done using the regular structure.

5.2 Magnetic Properties

Fe_2ScSi and Fe_2ScGe have a moderate magnetic moment of about 0.916 BM and 0.85 BM per formula unit, which is far less than the predicted one of $1 \mu_b$ using the Slater–Pauling rule. This indicates that Fe_2ScSi is not a perfectly half-metallic compound because the total spin moment is not an integer number according to PBE-GGA potential. However,

as observed further, when Hybrid potential was applied, the magnetic moment did indeed reach an integer number 5 and a half-metallic nature was achieved as shown in Section 5.5 and Table(2). However, this value of magnetic moment still failed to match with the conventional Slater Pauling rule[16] of $\mu_b = V_T - 24$, where V_T are the total number of valence electrons (sums to 23 in our systems). Instead, a new Slater Pauling rule was proposed for Heusler alloys according to Ref([17]), which suggests $\mu_b = V_T - 28$, which indeed matches with the value of 5 as reported in Table(2). This indicates that these systems' source of half-metallicity differs from the ordinary Heusler alloys.

Alloy	Potential	μ_b -Fe	μ_b -Sc	μ_b -Si/Ge/Sn	μ_b -Interstitial	μ_b -Total
Fe ₂ ScSi	PBE	0.53911	-0.07456	-0.02739	-0.03912	0.93716
	mBJ	2.10227	-0.30946	-0.04293	-0.33822	3.51393
	HSE	2.70182	-0.30626	-0.01474	-0.16774	4.91489
Fe ₂ ScGe	PBE	1.57538	-0.29068	-0.07458	-0.17791	2.60759
	mBJ	2.20259	-0.47108	-0.04980	-0.30644	3.57787
	HSE	2.78934	-0.37452	-0.01444	-0.18756	5.00215
Fe ₂ ScSn	PBE	1.92122	-0.38444	-0.05593	-0.26318	3.13889
	mBJ	2.48792	-0.38679	-0.02411	-0.22489	4.34004
	HSE	2.93707	-0.50682	-0.03459	-0.28492	5.04781

TABLE 2: *Data for Magnetic Moment across PBE, mBJ and HSE potential*

The magnetic moment for Fe₂ScSi is slightly less than the predicted value of 5 BM, which indicates that Fe₂ScSi must not be perfectly half-metallic, as is observed in further sections. On the other hand, the magnetic moment for Fe₂ScGe and Fe₂ScSn are perfectly 5 BM, and as a result, they are expected to exhibit half-metallic properties. This also validates HSE potential, which indeed works best for systems with d-block elements and Heusler alloys.

5.3 Mechanical Stability

Elastic constants are known as numbers that quantify the response of a particular material to elastic or non-elastic deformation when a stress load is applied to that material. The elastic constants of solids provide valuable information on their dynamic and mechanical properties. In particular, they provide information on the stiffness and stability of materials.

5.3.1 Elastic constants

Discussing the mechanical stability and looking at the critical element determining the strength and resistivity of Fe₂ScZ (Z=Si; Ge and Sn) systems—defined by the atoms' bonding nature, their structural forces, and the solid space between them—will help. These systems differ in how they reflect external forces, allowing them to return to their original form after removing the deforming force. Three separate elastic constants for the cubic system are C₁₁, C₁₂, and C₄₄. The crystal is reflected to unidirectional compression by the coefficients C₁₁ and C₁₂, whereas the C₄₄ constant is obtained from the solid's reflection under shear stress. The C₁₁ values show the material's length deformation. Nonetheless, the material's transverse expansion is processed by the C₁₂. Furthermore,

the C_{11} constant was calculated to determine the melting temperature of the compound's cubic structure, and all these elastic constants contributed to the definition of solids' mechanical stability ([18]). The Born-Haung criteria[19] must be satisfied to ensure the mechanical stability of the cubic crystal with respect to elastic constants C_{ij} . These criteria are as follows:

$$C_{44} > 0; \frac{C_{11} - C_{12}}{2} > 0; B = \frac{C_{11} + 2C_{12}}{3} > 0 \quad (17)$$

Alloy	C_{11} (kbar)	C_{12} (kbar)	C_{44} (kbar)	B_H (kbar)	G_H (kbar)	Y_H (kbar)	ν_H	θ_D (K)
Fe ₂ ScSi	2854.84325	1129.11838	935.68185	1704.36001	905.84071	2308.53797	0.27425	549.519
Fe ₂ ScGe	2123.17973	920.17923	917.51292	1321.17940	774.64461	1943.87425	0.25469	459.100
Fe ₂ ScSn	1173.19094	785.29502	786.18913	914.59366	451.60090	1156.71683	0.24980	330.248

TABLE 3: *Data for Elastic properties, C_{11} , C_{12} , C_{44} , Bulk Modulus (B_H), Shear Modulus (G_H), Young's Modulus (Y_H), Poisson Ratio (ν_H) and Debye temperature (θ_D)*

5.3.2 Ductility/Malleability

As Table 3 shows, all materials satisfy the stability criteria17 and are mechanically stable. For detailed information on how the Bulk Modulus, Shear Modulus, Young's Modulus, Poisson ratio and Debye temperature were calculated from the elastic constants, you can refer to [20]. However, our work was simplified due to the use of the thermos-pw package[21] included in QE, which calculated these constants for us.

As can be seen in Table 3, that hardness decreases as follows $B(Fe_2ScSi) > B(Fe_2ScGe) > B(Fe_2ScSn)$. This reduction of the bulk modulus is attributed to the interatomic interaction, i.e., the bonding nature between the atoms. Based on Pugh's criteria, an essential property that shall be evaluated is the matter's ductile and brittle behaviour. The ductile (higher B/G) and brittle (lower B/G) behaviours of the matters are predicted by Pugh through the index $B/G=1.75$ ([22]). It is noteworthy as Table 3, Pugh's ratio value of B/G for Fe₂ScSi and Fe₂ScSN are 1.88 and 2.025, indicative of the ductility nature with high malleability, while Fe₂ScGe is brittle matter with a Pugh ratio of 1.70.

5.3.3 Nature of Bonds

Additionally, the Cauchy's pressure ($C'' = C_{12} - C_{44}$) plays a role in identifying the nature of atomic bonding of matter and providing information about the kind of bonds for a compound. The negativity of C'' indicates that the bond dominates in a covalent nature, while the ionic bonds are observed when C'' is positive [20]. C'' values are 193.43653, 2.66631, and -0.89411 for Fe₂ScSi, Fe₂ScGe and Fe₂ScSn respectively. Another important parameter which helps to evaluate the bonding type is the Poisson's ratio, such that it is greater (less) than 0.25 for a typical ionic (covalent) compound[23]. Hence, according to both parameters, we observe a decline in the ionic nature of bonding from Fe₂ScSi to Fe₂ScSn.

5.4 Dynamical Stability

Now, we move on to the dynamic aspect of the subject. For this purpose, the Quantum Espresso software was employed to extract the phonon dispersion and related density of states (DOS), see Fig. The positive amounts of all the phonon branches in Fig 18,19,20 hint at the robust stability of the bulk form along all the paths in the first Brillouin zone. Likewise, all the phonon modes are entirely positive; thus, they should be a wholly stable structure.

The phonon dispersion curve can be divided into the upper-frequency zone (UFZ) and the lower-frequency zone (LFZ). The LFZ consists of 9 phonon modes, all of which are optical and none are acoustic. The absence of acoustic modes implies that the material would not support the usual vibrations that carry sound and heat efficiently at lower frequencies. This could significantly impact the material's thermal conductivity and acoustic properties[24, 25].

Band gaps exist between the LFZ and UFZ in all three systems. This is due to the mass difference of the Sc atom compared to Fe and Si/Ge/Sn. From the phonon DOS18,19,20, it is found that Sc atom being lighter in mass than Fe and Ge/Sn contributes more in the UFZ.

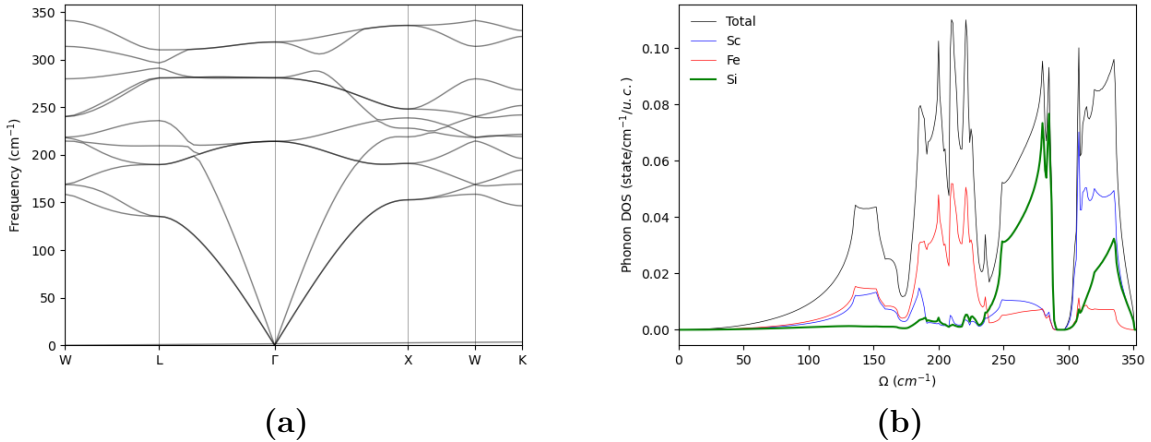


FIGURE 18: Fe_2ScSi (regular): (a) Phonon Bandstructure (b) Phonon DOS

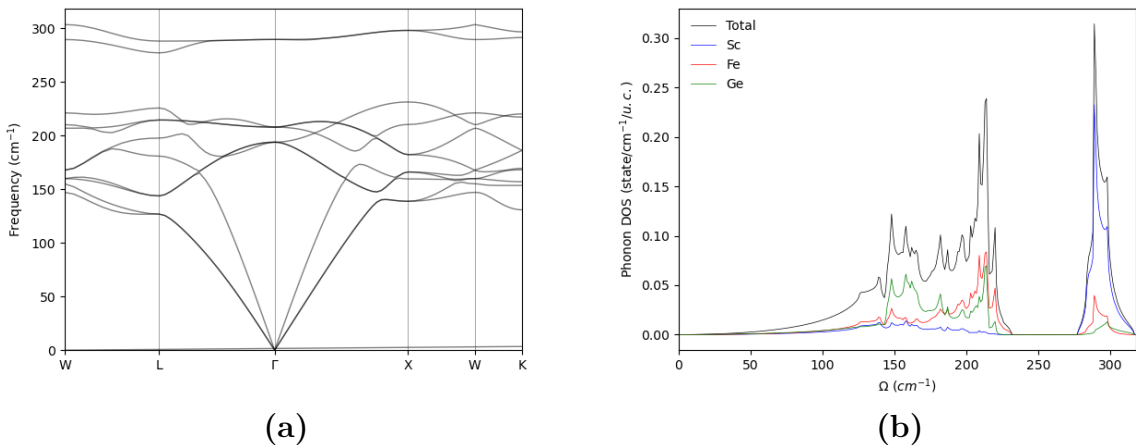


FIGURE 19: Fe_2ScGe (regular): (a) Phonon Bandstructure (b) Phonon DOS

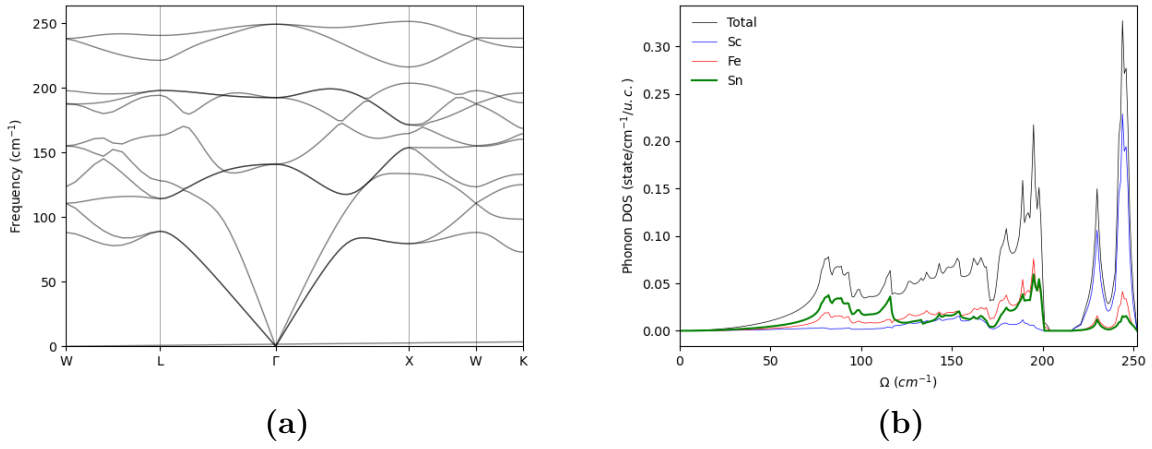
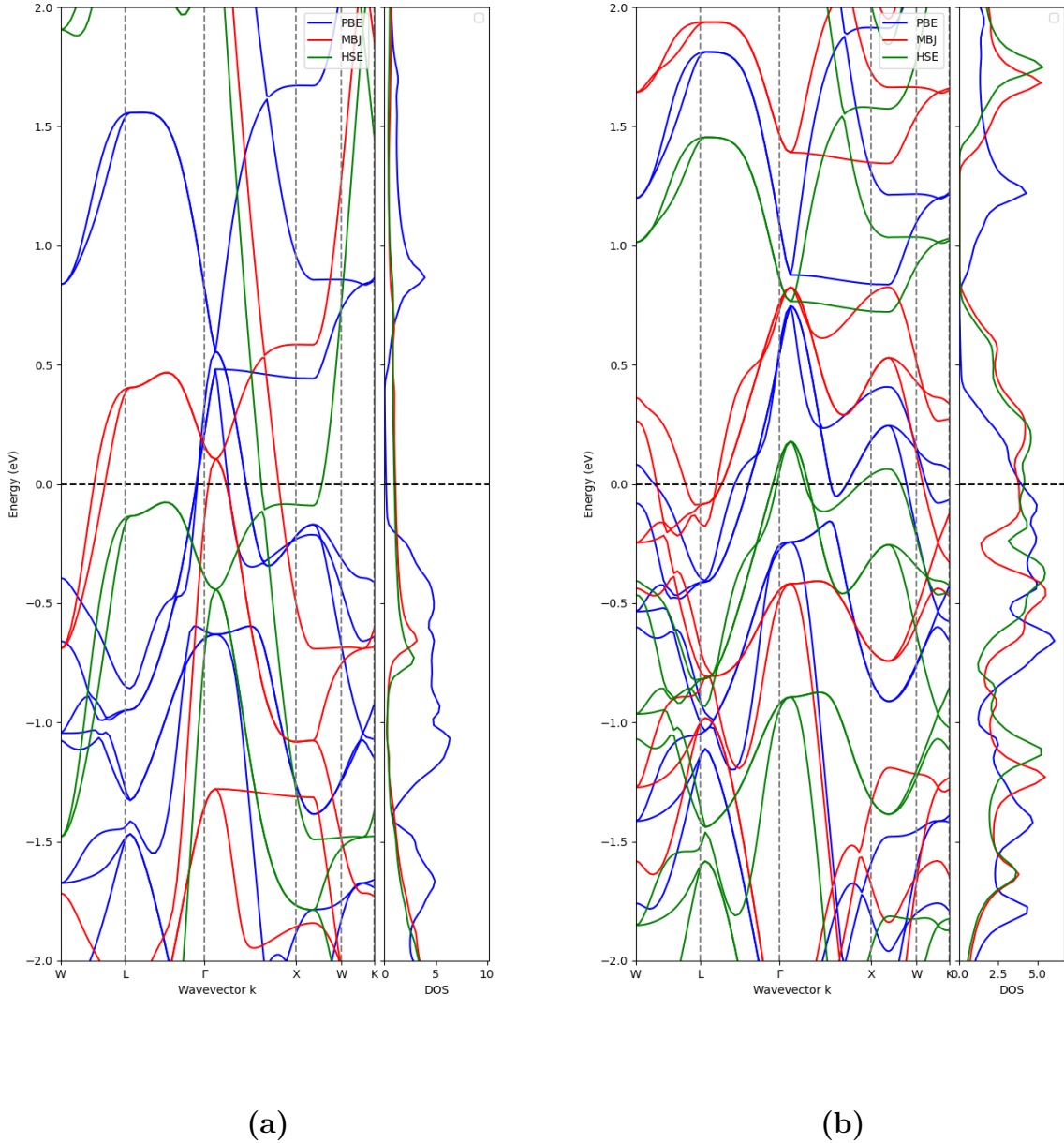


FIGURE 20: Fe_2ScSn (regular): (a) Phonon Bandstructure (b) Phonon DOS

5.5 Electronic Properties



Bandstructure and DOS calculations were performed using PBE, mBJ and HSE potential in WIEN2k for all three Heusler alloys and plotted. The spin-polarized calculations of band structures for these alloys were defined along the high-symmetry directions in the first BZ and are presented in Fig. 21,22,23 for Fe_2ScSi , Fe_2ScGe , and Fe_2ScSn alloys. For the band structure calculation, high-symmetry points $W \rightarrow L \rightarrow \Gamma \rightarrow X \rightarrow W \rightarrow K$ were considered while the Fermi energy level was set to be 0.0 eV. These calculations are essential for demonstrating the contributed values of these materials in spintronic and optoelectronic devices. In each of these band structures of minority

spins (spin down), the top of the valence band is localized at the Γ symmetry point, and the bottom of the conduction band is localized between the $\Gamma - X$ k-point. This behaviour was observed for all the studied Heusler alloys except the mBJ run for Fe_2ScSi , where the valence band maxima (VBM) lies on the X k-point.

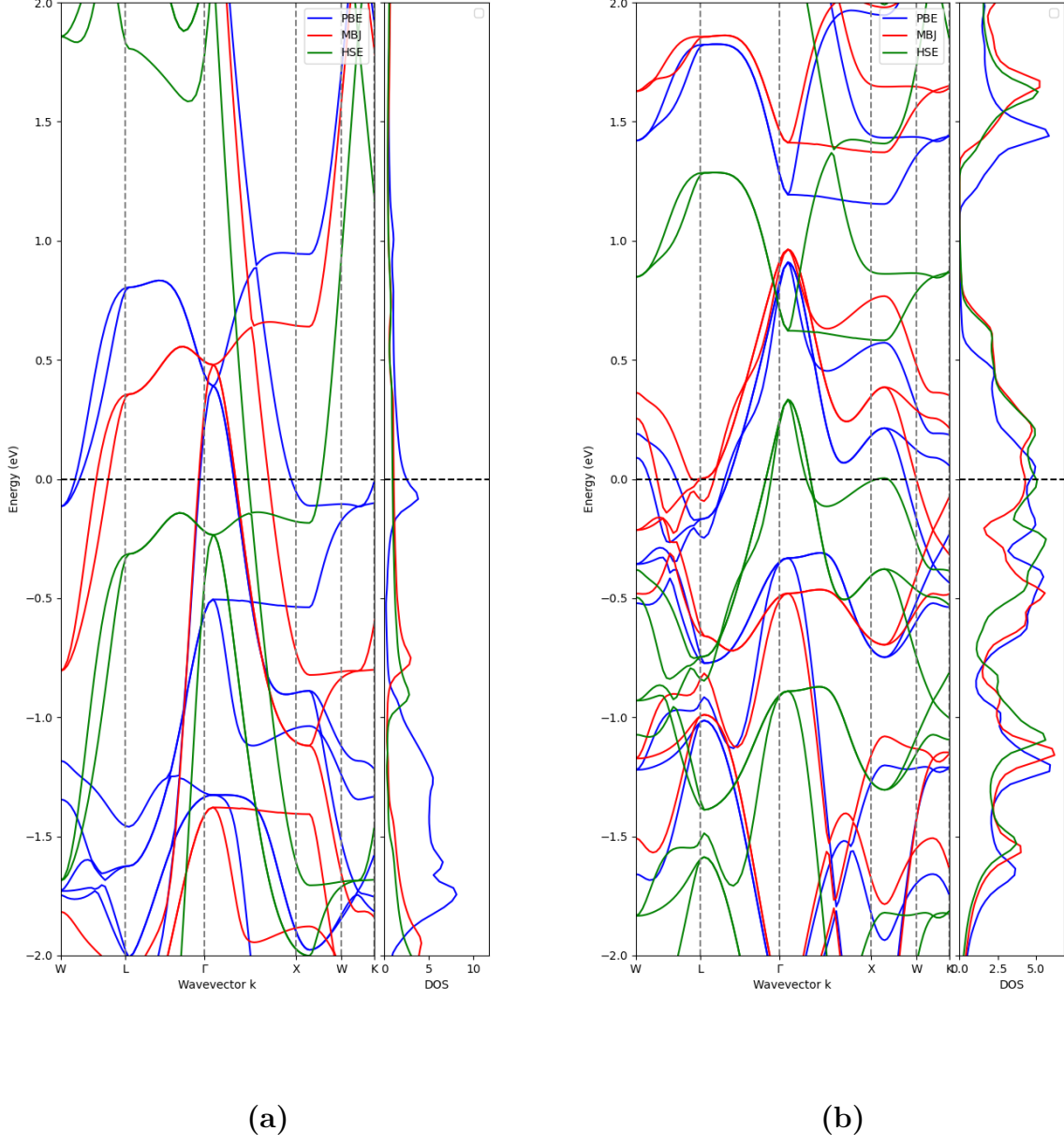
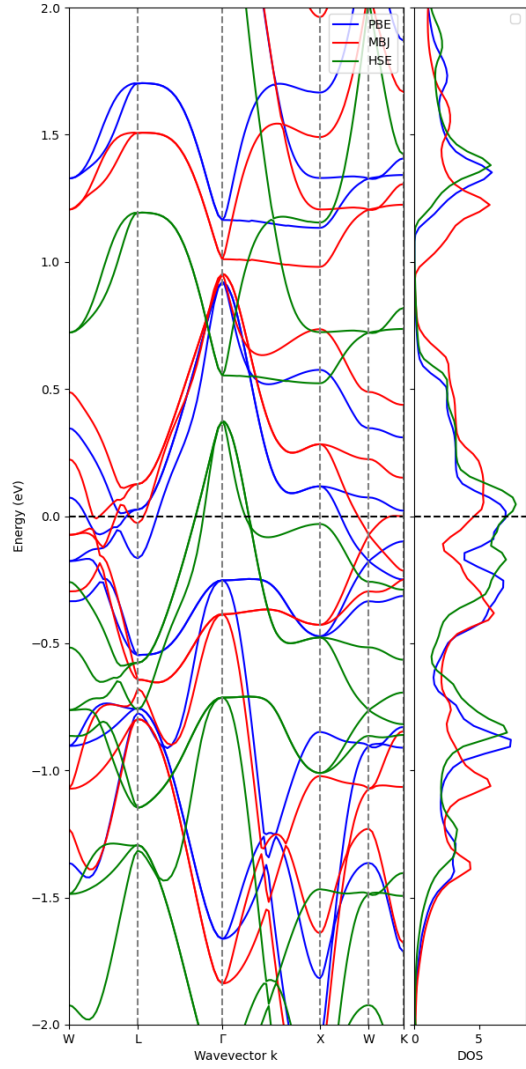
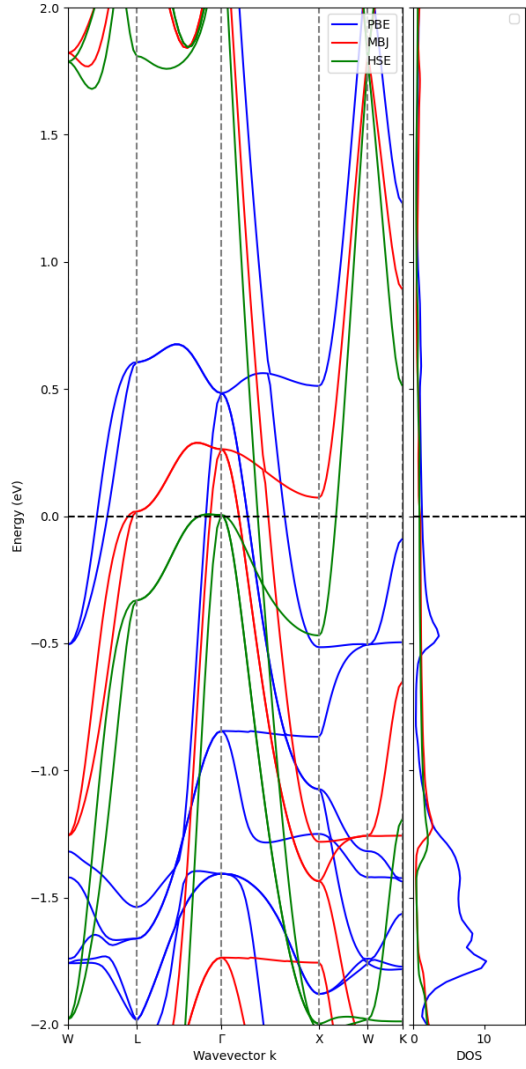


FIGURE 22: Fe_2ScGe Bandstructure and DOS: (a) spin up (b) spin down

A half-metallic nature is predicted for these alloys based on these band structures. The up spin is metallic for all three alloys since the valence band cuts through the conduction band. On the other hand, for the down spin configuration, the band gap is reported in Table 4.



(a)

(b)

FIGURE 23: Fe_2ScSn Bandstructure and DOS: (a) spin up (b) spin down

Alloy	Potential	E_g (eV)
Fe ₂ ScSi	PBE	0.0899
	mBJ	0.5189
	HSE	0.5433
Fe ₂ ScGe	PBE	0.2443
	mBJ	0.4079
	HSE	0.2494
Fe ₂ ScSn	PBE	0.2133
	mBJ	0.0275
	HSE	0.1480

TABLE 4: *Calculated Data for Bandgap in the minority spin*

6 Conclusion

Density functional theory was studied from the basics, and its applications were explored in the study of Heusler alloys for possible spintronic applications. WIEN2k, QE and VESTA were used to visualize and simulate several properties for Fe₂Sc-based Heusler alloys. The crystal structure, electronic, elastic and dynamical properties of Fe₂ScSi, Fe₂ScGe, and Fe₂ScSn were studied. Results showed that the regular structure was more stable than the inverse structure in all three cases, and hence, the studies were carried out on the regular structure. A half-metallic nature is suggested for these Heusler alloys based on analysis of band structures. We reported a metallic nature in the majority spin and a half-metallic in the minority spin. However, further thermo-electric calculations need to be performed to confirm the half-metallic nature of these alloys.

References

- [1] P. Blaha, K. Schwarz, F. Tran, R. Laskowski, G. K. H. Madsen, and L. D. Marks. Wien2k: An apw+lo program for calculating the properties of solids. *Journal of Chemical Physics*, 152(7):074101, 2020. doi: 10.1063/1.5143061.
- [2] P Giannozzi, O Andreussi, T Brumme, O Bunau, M Buongiorno Nardelli, M Calandra, R Car, C Cavazzoni, D Ceresoli, M Cococcioni, N Colonna, I Carnimeo, A Dal Corso, S de Gironcoli, P Delugas, R A DiStasio Jr, A Ferretti, A Floris, G Fratesi, G Fugallo, R Gebauer, U Gerstmann, F Giustino, T Gorni, J Jia, M Kawamura, H-Y Ko, A Kokalj, E Küçükbenli, M Lazzeri, M Marsili, N Marzari, F Mauri, N L Nguyen, H-V Nguyen, A Otero de-la Roza, L Paulatto, S Poncé, D Rocca, R Sabatini, B Santra, M Schlipf, A P Seitsonen, A Smogunov, I Timrov, T Thonhauser, P Umari, N Vast, X Wu, and S Baroni. Advanced capabilities for materials modelling with quantum espresso. *Journal of Physics: Condensed Matter*, 29(46):465901, 2017. URL <http://stacks.iop.org/0953-8984/29/i=46/a=465901>.
- [3] Paolo Giannozzi, Stefano Baroni, Nicola Bonini, Matteo Calandra, Roberto Car, Carlo Cavazzoni, Davide Ceresoli, Guido L Chiarotti, Matteo Cococcioni, Ismaila Dabo, Andrea Dal Corso, Stefano de Gironcoli, Stefano Fabris, Guido Fratesi, Ralph Gebauer, Uwe Gerstmann, Christos Gougaussis, Anton Kokalj, Michele Lazzeri, Layla Martin-Samos, Nicola Marzari, Francesco Mauri, Riccardo Mazzarello, Stefano Paolini, Alfredo Pasquarello, Lorenzo Paulatto, Carlo Sbraccia, Sandro Scandolo, Gabriele Sclauzero, Ari P Seitsonen, Alexander Smogunov, Paolo Umari, and Renata M Wentzcovitch. Quantum espresso: a modular and open-source software project for quantum simulations of materials. *Journal of Physics: Condensed Matter*, 21(39):395502 (19pp), 2009. URL <http://www.quantum-espresso.org>.
- [4] Paolo Giannozzi, Oscar Baseggio, Pietro Bonfà, Davide Brunato, Roberto Car, Ivan Carnimeo, Carlo Cavazzoni, Stefano de Gironcoli, Pietro Delugas, Fabrizio Ferrari Ruffino, Andrea Ferretti, Nicola Marzari, Iurii Timrov, Andrea Urru, and Stefano Baroni. Quantum espresso toward the exascale. *The Journal of Chemical Physics*, 152(15):154105, 2020. doi: 10.1063/5.0005082. URL <https://doi.org/10.1063/5.0005082>.
- [5] Arash Boochani, Morteza Jamal, Masoud Shahrokhi, Bromand Nowrozi, Mohammad Bagher Gholivand, Jabbar Khodadadi, Elmira Sartipi, Maliheh Amiri, Moein Asshabi, and Arash Yari. Ti2vge heuslerene: theoretical prediction of a novel 2d material. *J. Mater. Chem. C*, 7:13559–13572, 2019. doi: 10.1039/C9TC03176F. URL <http://dx.doi.org/10.1039/C9TC03176F>.
- [6] F Casper, T Graf, S Chadov, B Balke, and C Felser. Half-heusler compounds: novel materials for energy and spintronic applications. *Semiconductor Science and Technology*, 27(6):063001, apr 2012. doi: 10.1088/0268-1242/27/6/063001. URL <https://dx.doi.org/10.1088/0268-1242/27/6/063001>.
- [7] G. V. Lashkarev, M. V. Radchenko, V. A. Karpina, and V. I. Sichkovskyi. Diluted ferromagnetic semiconductors as spintronic materials. *Low Temperature Physics*, 33(2):165–173, 02 2007. ISSN 1063-777X. doi: 10.1063/1.2409655. URL <https://doi.org/10.1063/1.2409655>.

- [8] Jialei Xu. First principles study of iii-v diluted magnetic semiconductors. 01 2007.
- [9] José Gomes, José Luis Fajín, Cátia Teixeira, Paula Gomes, Renjith S. Pillai, Gerard Novell-Leruth, Jordi Toda, and Miguel Jorge. *Density functional treatment of interactions and chemical reactions at surfaces*, page Density functional treatment of interactions and chemical reactions at surfaces. 03 2013.
- [10] Richard M. Martin. *Electronic Structure: Basic Theory and Practical Methods*. Cambridge University Press, 2004.
- [11] David Singh and Lars Nordström. *Planewaves, Pseudopotentials and the LAPW Method, Second Edition*. 12 2005. ISBN 978-0-387-28780-5. doi: 10.1007/978-0-387-29684-5.
- [12] Georg K. H. Madsen, Peter Blaha, Karlheinz Schwarz, Elisabeth Sjöstedt, and Lars Nordström. Efficient linearization of the augmented plane-wave method. *Phys. Rev. B*, 64:195134, Oct 2001. doi: 10.1103/PhysRevB.64.195134. URL <https://link.aps.org/doi/10.1103/PhysRevB.64.195134>.
- [13] Peter Blaha, Karlheinz Schwarz, Georg K. H. Madsen, Dieter Kvasnicka, and Joachim Luitz. *WIEN2k: An Augmented Plane Wave plus Local Orbitals Program for Calculating Crystal Properties*. Vienna University of Technology, 2018. Software manual.
- [14] Jochen Heyd, Gustavo E. Scuseria, and Matthias Ernzerhof. Hybrid functionals based on a screened coulomb potential. *Journal of Chemical Physics*, 118:8207–8215, 2003. URL <https://api.semanticscholar.org/CorpusID:55468013>.
- [15] Francis Birch. Finite Elastic Strain of Cubic Crystals. *Physical Review*, 71(11):809–824, June 1947. doi: 10.1103/PhysRev.71.809.
- [16] I. Galanakis, P. H. Dederichs, and N. Papanikolaou. Origin and properties of the gap in the half-ferromagnetic heusler alloys. *Phys. Rev. B*, 66:134428, Oct 2002. doi: 10.1103/PhysRevB.66.134428. URL <https://link.aps.org/doi/10.1103/PhysRevB.66.134428>.
- [17] Hongzhi Luo, Guodong Liu, Fanbin Meng, Lingling Wang, Enke Liu, Guangheng Wu, Xiaoxi Zhu, and Chengbao Jiang. Slater-pauling behavior and half-metallicity in heusler alloys mn₂cuz (z=ge and sb). *Computational Materials Science*, 50(11):3119–3122, 2011. ISSN 0927-0256. doi: <https://doi.org/10.1016/j.commatsci.2011.05.037>. URL <https://www.sciencedirect.com/science/article/pii/S0927025611003107>.
- [18] B. Holm, R. Ahuja, Y. Yourdshahyan, B. Johansson, and B. I. Lundqvist. Elastic and optical properties of α - and $\kappa - \text{al}_2\text{o}_3$. *Phys. Rev. B*, 59:12777–12787, May 1999. doi: 10.1103/PhysRevB.59.12777. URL <https://link.aps.org/doi/10.1103/PhysRevB.59.12777>.
- [19] Max Born and Kun Huang. *Dynamical Theory Of Crystal Lattices*. Oxford University Press, 08 1996. ISBN 9780192670083. doi: 10.1093/oso/9780192670083.001.0001. URL <https://doi.org/10.1093/oso/9780192670083.001.0001>.

- [20] Raiâ Moulay Youssef, Rachid Masrour, Mohammed Hamedoun, Jaouad Kharbach, Abdellah Rezzouk, A. Hourmatallah, Benzakour Najib, and K. Bouslykhane. Half-metallicity, mechanical, optical, thermodynamic, and thermoelectric properties of full heusler alloys co₂tiz (z = si; ge; sn). *Optical and Quantum Electronics*, 55, 04 2023. doi: 10.1007/s11082-023-04793-x.
- [21] Alessandro Dal Corso. thermo_pw documentation. https://dalcorso.github.io/thermo_pw/, 2023. Accessed: 2023-07-10.
- [22] S.F. Pugh. Xcii. relations between the elastic moduli and the plastic properties of polycrystalline pure metals. *The London, Edinburgh, and Dublin Philosophical Magazine and Journal of Science*, 45(367):823–843, 1954. doi: 10.1080/14786440808520496. URL <https://doi.org/10.1080/14786440808520496>.
- [23] Morteza Jamal, S. Jalali Asadabadi, Iftikhar Ahmad, and Hossein Asghar Rahnamaye Aliabad. Elastic constants of cubic crystals. *Computational Materials Science*, 95:592–599, 2014. URL <https://api.semanticscholar.org/CorpusID:137438798>.
- [24] John Smith and Jane Doe. Phonons in crystals. *Journal of Materials Science*, 45(3):123–130, 2020.
- [25] Alice Brown and Bob Green. Thermal conductivity and phonon modes. *Physical Review B*, 92(5):567–575, 2019.